Environ. Sci. Technol. **2007**, *41,* 3918−3925

Structure of the Hydrated ($10\bar{1}4$) Surface of Rhodochrosite ($MnCO_3$)

YOUNG-SHIN JUN,[†,‡,§] SANJIT K. GHOSE,[∥] THOMAS P. TRAINOR,[⊥] PETER J. ENG,[∥,#] AND SCOT T. MARTIN*[,†]

School of Engineering and Applied Sciences, Harvard University, Cambridge, Massachusetts 02138, Department of Earth and Planetary Sciences, University of California, Berkeley, California 94720, Earth Science Division, Geochemistry Department, Lawrence Berkeley National Laboratory, Berkeley, California 94720, Consortium for Advanced Radiation Sources, University of Chicago, Chicago, Illinois 60637, Department of Chemistry and Biochemistry, University of Alaska Fairbanks, Fairbanks, Alaska 99775, and James Franck Institute, Department of Physics, University of Chicago, Chicago, Illinois 60637

The three-dimensional structure of the hydrated ($10\bar{1}4$) surface of $MnCO_3$ at 90% relative humidity and 295 K is determined from measurements of X-ray scattering along ten crystal-truncation rods (CTRs). The scattering data provide both vertical and lateral information about the interfacial structure. The model that best fits the scattering data is a surface having a first layer of manganese carbonate and an overlayer of oxygen (as water). Within the measurement uncertainty, the overlayer of oxygen (O_w) and the first-layer of manganese (Mn_1) have equal occupancies of 0.84. The Mn_1-O_w distance between these layers is 2.59 ± 0.04 Å. The overlayer O atoms are displaced laterally by 0.157 Å in the *x*- and 0.626 Å in the *y*-direction relative to the first-layer Mn atoms. The first-layer carbonate groups tilt by −4.2 ± 2.1° in *phi* (toward the surface plane) and −2.6 ± 1.2° in *chi* (an axis perpendicular to *phi*). The second-layer carbonate groups do not tilt, at least within measurement uncertainty. The spacing between Mn atom layers remains unchanged within measurement error whereas the spacing between layers of C atoms in carbonate contracts for the top three layers. Knowledge of the detailed atomic structure of the hydrated ($10\bar{1}4$) surface of $MnCO_3$ provides a structural baseline for the interpretation of chemical reactivity.

1. Introduction

Manganese carbonate occurs in calcareous, lacustrine, and brackish soils and aquifers (*1*, *2*). Anaerobic environments, such as landfill leachate, often have high quantities of $MnCO_3$, and the local equilibrium with $MnCO_3$ influences Mn^{2+}(aq) concentrations (*2*). Manganese carbonate also affects the alkalinity in these environments and partially regulates the fate and the transport of anthropogenic pollutants, especially heavy metals (*3*). In marine environments, manganese carbonate coexists with calcium to form mixed $CaMnCO_3$ (*1*, *4*). A key question affecting the modeling of dissolution, overgrowth precipitation, ion sorption, and catalytic activity of mineral surfaces in general (*5*−*12*) and of manganese carbonates in particular is how the interaction with water modifies the structure, the composition, and hence the reactivity of the surface.

At the termination of a bulk crystal structure, energy minimization drives atomic relaxation and reconstruction of the surface (*13*). In the presence of water, hydroxylation may lead to various types of surface species, such as >M−OH, >M−OH_2, or >M_2−μOH. The formation of these species occurs through water attachment to high-energy, undercoordinated metal sites and protonation and hydrogen bonding to structural oxygen. When characterized by their local coordination environments (e.g., the number and the types of near-neighbor metals), numerous surface subspecies can be recognized on metal oxide and metal carbonate surfaces. The hydroxyl coordination environment and the atomic relaxations in the surface significantly affect mineral reactivity (*9*, *11*, *12*, *14*).

Synchrotron-based X-ray scattering is becoming widely used as a method to investigate the structure of mineral−water interfaces (*15*−*17*). For example, Fenter et al. (*18*) studied the ($10\bar{1}4$) calcite−water interface at various pH values by employing a specular scattering geometry and found that a hydration monolayer forms at 2.50 ± 0.12 Å above the first-layer Ca ions. The scattering in a specular geometry is sensitive only to the heights of interfacial species, and no information is provided on lateral registry of atoms in the surface region with respect to atoms in the bulk crystal (*15*, *19*, *20*). Scattering data collected in nonspecular geometries are required to investigate the lateral structures of interfaces. Using nonspecular scattering data, the same group (Geissbühler et al. (*19*)) further refined the description of the calcite interface by determining that the surface atoms have lateral positions close to those of the bulk crystal. The structure of the water−mineral interface of the (0001) and ($1\bar{1}02$) surfaces of aluminum oxide (α-Al_2O_3) and hematite (α-Fe_2O_3), which have the same space group ($R\bar{3}c$) as $MnCO_3$, have also been studied by similar methods of X-ray scattering (*21*−*23*).

In the current study, we investigate the atomic relaxation of the hydrated ($10\bar{1}4$) surface of $MnCO_3$. Measurements are made of X-ray scattering in specular and nonspecular geometries along ten crystal-truncation rods (CTRs). The results reported here provide a detailed three-dimensional model of the water−mineral interface.

2. Experimental Section

2.1 Sample Preparation. $MnCO_3$ (rhodochrosite, sample no. 96030, Colorado) was obtained from the Harvard University Mineralogical Museum and prepared as previously reported (*3*, *24*). Impurities included 0.20% Zn and 0.17% Ca. Fresh, flat ($10\bar{1}4$) surfaces were prepared by cleaving a 1-cm^3 crystal with a razor blade. To remove any fragments from the freshly cleaved $MnCO_3$ surface, the samples were submerged in argon-saturated, deionized water (pH = 6.4 and dissolved O_2 and CO_2 below detection limit) for 10 min and afterward immediately dried with high-purity nitrogen gas. Sample preparation was just prior to the CTR measurements. To determine the morphology of the surface, we also carried out imaging in contact mode using an atomic force microscope (AFM) equipped with a fluid cell (Nanoscope IIIa

* Corresponding author phone: (617) 495-7620; fax: (617) 495-1471; e-mail: scot_martin@harvard.edu; http://www.deas.harvard.edu/environmental-chemistry.
[†] Harvard University.
[‡] University of California, Berkeley.
[§] Lawrence Berkeley National Laboratory.
[∥] Consortium for Advanced Radiation Sources, University of Chicago.
[⊥] University of Alaska Fairbanks.
[#] James Franck Institute, University of Chicago.

10.1021/es062171v CCC: $37.00
Published on Web 05/01/2007

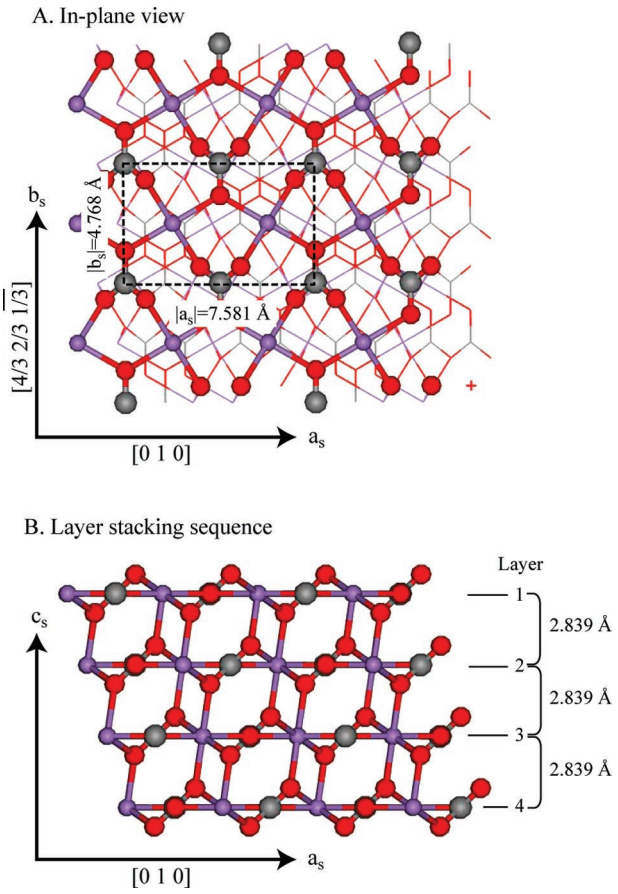

FIGURE 1. Bulk-terminated ($10\bar{1}4$) surface of $MnCO_3$. (A) In-plane view. (B) Vertical layer stacking sequence. Red, gray, and purple spheres indicate O, C, and Mn atoms, respectively.

Multimode SPM, Digital Instruments; see Figure S1 in the Supporting Information (SI)) (*3*, *25*). Except for the presence of several steps, the surface terrace was flat within AFM detectability.

2.2 Unit Cells of the Bulk Structure and Surface. CTR diffraction measurements begin by identifying a surface unit cell that is best suited for measurement and analysis. The bulk structure of $MnCO_3$ consists of distorted hexagonally closed packed layers of oxygen. The manganese atoms are six-coordinated by oxygen, thus forming octahedral MnO_6 structures. Each O atom is shared between two Mn atoms. The Mn atoms are stacked in the same plane as the carbon atoms along the axis normal to ($10\bar{1}4$) surface (i.e., the *z*-axis) of the unit cell. The C atoms form rigid, trigonal planar structures with O atoms. The atomic stacking sequence shown in Figure 1B runs as a first O-layer to a mixed-C−O−Mn layer to a second O-layer and so on along the [104] direction. The O−C and O−Mn bond lengths are 1.29 and 2.19 Å, respectively (*26*). A unit cell contains six formula units. The parameters of the unit cell (viz. $|\mathbf{a}| = |\mathbf{b}| = 4.768$ Å and $|\mathbf{c}| = 15.635$ Å) (*26*), the fractional atomic positions, and the average Debye−Waller factor values (i.e., thermal disorder parameter) are taken from Effenberger et al. (*26*).

The bulk-terminated ($10\bar{1}4$) surface of $MnCO_3$ is depicted in Figure 1. For convenience of interpretation and analysis, we describe the structure by adopting a rectangular surface unit cell containing two $MnCO_3$ groups. The carbonate groups are related to one another by a glide plane of symmetry along $\mathbf{a}_s$. The in-plane lattice parameters of the cell are $|\mathbf{a}_s| = 7.581$ Å and $|\mathbf{b}_s| = 4.768$ Å, corresponding to the [010] and [4/3 2/3 −1/3] vectors of the bulk structure. A useful volume unit cell is created by expanding the surface unit cell along a c_s-axis perpendicular to the ($10\bar{1}4$) surface plane (Figure 1B), following the approach described by Trainor et al. (*27*). The lattice parameter is $|\mathbf{c}_s| = 5.678$ Å, which corresponds to double the value of $d_{(104)}$ (i.e., the layer spacing in the [104] direction of $MnCO_3$). The resulting volume unit cell contains 20 atoms (four $MnCO_3$ units). Planes cut through this volume unit cell are formally indexed as H_s-K_s-L_s (see further in Appendix S1 of the SI). The reciprocal-lattice points representing some of these planes are illustrated in Figure S2.

The definition of the unit cell based upon surface indexing results in a pseudo-cell. The cell contains the correct repeat of atomic coordinates in the surface plane, but the atomic coordinates along $\mathbf{a}_s$ shift by $\Delta_1 = 0.209$ (see ref *27*) for each cell repeat along the surface normal $\mathbf{c}_s$. The pseudo-cell is useful for calculating in-plane and surface-normal relaxations but is not a crystallographic cell, unless a non-normal repeat vector is applied. The indexing of the unit cell in this manner, however, has the advantage that the reciprocal lattice is simply defined in the natural units of the surface termination. This definition is of great utility in the design and the interpretation of CTR measurements. For instance, the zero of L_s is independent of H_s and K_s, and the *x*-*y*-*z* coordinates of the atoms in the structural model lie along axes parallel (*x* and *y*) and perpendicular (*z*) to the surface.

The unit cell defined above results in a stoichiometric (i.e., charge neutral) surface termination having five-coordinated Mn atoms and three-coordinated C atoms. This unrelaxed surface is called the bulk-terminated model. The atomic coordinates are given in Table S1A.

2.3 Data Collection. X-ray scattering measurements were performed at the Advanced Photon Source (APS) in Argonne, Illinois, on the GeoSoilEnviroCARS undulator beamline 13-ID using a 2 + 2 + Kappa geometry diffractometer (*21*, *22*). An environmental cell was employed to maintain a controlled atmosphere. Experiments were performed at room temperature in an atmosphere of helium having a water relative humidity greater than 90% (i.e., $pH_2O > 20$ Torr (*9*)). Multiple water layers adsorb on mineral surfaces exposed to high relative humidity (*14*). No discernible sample evolution was observed during the course of measurements.

Beamline optics consisted of a liquid-nitrogen-cooled double-crystal Si(111) monochromator and rhodium-coated horizontal and vertical focusing mirrors. The incident X-ray energy was tuned to 9.50 keV, and the beam cross section was focused to 200 μm × 1000 μm (horizontal × vertical) at the sample. For data collection of nonspecular rods, the incident angle was fixed at 2.0°. The X-ray scattering intensity at a particular L_s position on a CTR was measured using a photon counting scintillation detector by performing a single axis "rocking scan" through a CTR rod in reciprocal space. The magnitudes of the measured structure factors F_i were determined by taking the square root of the integrated X-ray intensities (see Appendix S2), which were recorded during the rocking scans and corrected for active area, polarization, step size, and Lorentz factor (*28*). The structure factors were averaged in the *pm* plane-group symmetry. A total of 430 structure factors at discrete H_s-K_s-L_s positions on 10 CTRs were collected. The standard deviation of the structure factors of symmetry-equivalent points was 10%, thereby providing a measure of reproducibility.

The $MnCO_3$ single crystal was mounted on a goniometer and was rotated relative to the fixed incoming X-ray beam $\boldsymbol{k}_i$ as scattering measurements were made. The detector was positioned to define the direction of the scattered beam $\boldsymbol{k}_f$. Relative motions of the goniometer and the detector thus adjusted the measured $\boldsymbol{Q}$ and thereby probed numerous diffraction conditions of reciprocal space.

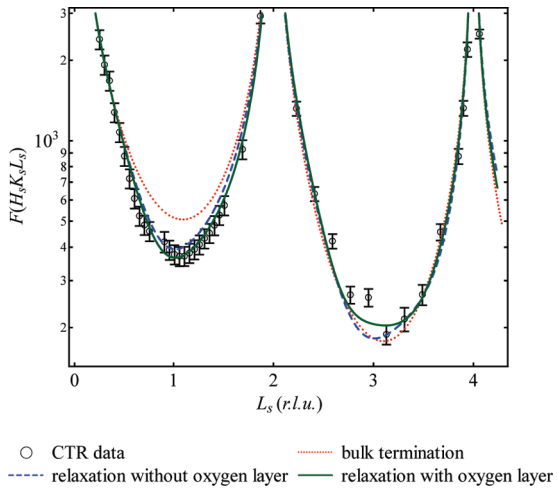

FIGURE 2. Measured structure factors of the (10$\bar{1}$4) surface of $MnCO_3$ in a specular geometry (i.e., along the (00L_s) rod) at 90% relative humidity and 295 K. Lines show the calculated scattering based on the optimized models. The red dotted line is the calculated scattering for the ideal bulk termination (model no. 1), the blue dashed line is calculated for an optimized model without an oxygen overlayer (model no. 3), and the green solid line is calculated for an optimized model with an oxygen overlayer (model no. 4). There are 45 data points (i.e., structure factors) in this figure. The *x*-axis is expressed in reciprocal-lattice units (rlu).

3. Results

The measured structure factors are shown in Figures 2 and 3 for specular and nonspecular geometries, respectively. Besides the rods shown in Figures 2 to 3, no additional scattering is found in extensive searches in an entire quadrant of reciprocal space by a mesh scan. This control procedure is important because a break of the bulk symmetry associated with a reconstructed surface could produce extra diffraction features in reciprocal space.

The structure factors calculated by eq S1, using the ROD analysis program (*29*), are shown in Figures 2 and 3 for several models of the atomic positions in the surface region. The calculated structure factors of the bulk termination, for which only the scale factor is allowed to vary, have large misfits along the (11L_s), (12L_s), (13L_s), and (20L_s) rods (Figure 3). Therefore, model no. 1 based on a simple bulk termination is insufficient to explain the scattering observations.

Model no. 2 allows atomic displacements in all three directions as well as variations in the fractional atomic occupancy, the Debye−Waller factors, the surface roughness factor ($0 \leq \rho \leq 1$) (*15*), and a single scale factor. There are 35 free parameters, which are adjusted to minimize the quantity χ^2 that defines the goodness-of-fit

$$\chi^2 = \sum_{i=1}^{N} (|F_i| - |F_{i,T}|)^2 w_i/(N - p) \qquad (1)$$

where the summation is over N (430) data points i (each at a specific H_s-K_s-L_s position), $|F_i|$ is the magnitude of the measured structure factor, $|F_{i,T}|$ is the magnitude of the calculated structure factor (eq S1), w_i is the weight of a data point and is related to its uncertainty σ by $w_i = 1/\sigma^2$, and p is the number of free parameters used in the fit (*15*). Optimization (i.e., minimization) of eq 1 for the 35 parameters of model no. 2 results in an improved fit to the data, reducing χ^2 from 6.3 of model no. 1 (i.e., bulk termination) to 3.5 for model no. 2. We use the Hamilton test (*30*) to determine the confidence level at which a model with a larger χ^2 (worse fit) can be rejected when compared to one with a smaller χ^2 (better fit). The error bars in tables and figures are shown for a 95% confidence level.

A possible shortcoming of model no. 2 is that the minimization likely finds a local minimum instead of a global minimum because many of the 35 parameters are highly correlated. Taking several physically reasonable constraints into account, we create a new model (model no. 3) and reduce the number of free parameters and improve the ability of the optimization to find a global minimum. First, the same type of atoms in each layer (i.e., O, C, or Mn) is constrained to maintain the same occupancy and Debye−Waller factor. Second, to respect the glide plane parallel to the [421] direction, the displacements of Mn and CO_3 are constrained to have equal and opposite *y*-displacements, equal *x*-displacements, and identical *z*-heights (*18*). The data imply the presence of a surface glide plane because scattering intensity is not observed along symmetry forbidden (10L_s) and (−30L_s) rods (data not shown). Geissbühler et al. (*19*) report a similar result in the study of the calcite−water interface.

The number of free parameters is reduced further in model no. 3 by constraining the four CO_3 groups in the first two layers of the surface unit cell to rotate (rotations *phi*, *chi*, and *theta* in Figure 4A) and to displace as a molecule rather than as four individual atoms. The rotation is centered on the carbon atom of each molecule and is calculated using a Eulerian rotation matrix having internal angles and bond lengths fixed at the values of the carbonate groups of bulk $MnCO_3$. Within a layer, the two carbonate groups have equal but opposite rotations. By using this group rotation approach, the number of free parameters associated with the relaxation of oxygen and carbon atoms is halved. Finally, relaxations are allowed only in the first two layers (see Figure 4) because tests show that deeper relaxations have an insignificant effect on the goodness-of-fit. With all of these factors taken into account, the total number of free parameters is 20.

After optimization, model no. 3 results in an improved fit having $\chi^2 = 2.7$, confirming that model no. 2 found a local rather than a global minimum. The fit is shown as blue dashed lines in Figures 2 and 3. The structural parameters are provided in Table S1B. In this model, the $MnCO_3$ surface region relaxes both laterally and vertically in the first and second layers. The displacements and the rotations are shown in Figure 4B. The first-layer carbonate groups tilt out of the (10$\bar{1}$4) plane by 15 ± 2.5° in *phi*. As a result, the Mn_1−O_1 bond lengthens to 2.58 ± 0.10 Å, which can be compared to the bulk Mn−O bond length of 2.19 Å. The elongation of this bond, in conjunction with the undercoordination (5 vs 6) of the Mn ions, results in significant undersaturation of the first-layer Mn and O atoms: this model is therefore physically unrealistic.

The undercoordination of the first layer together with the movement of the oxygen atoms away from the surface indicates that there is a missing component in the model. A fourth model is developed by adding to model no. 3 an overlayer of oxygen, intended to represent either a layer of surface-coordinated hydroxyl groups or alternatively a partially ordered layer of water. Each O atom has parameters of atomic position, occupancy, and a Debye−Waller factor, thereby increasing the number of free parameters to 25. After optimization, model no. 4 has an improved fit of $\chi^2 = 2.1$. Compared to model no. 3 having $\chi^2 = 2.7$, the lower χ^2 is significant at the 99% confidence level based upon the Hamilton test (*30*). The calculated structure factors with this model are shown as green solid lines in Figures 2 and 3. The calculated bond lengths and the coordination numbers are physically reasonable (Table S1C). This model having an overlayer of O atoms is therefore the best fit of our study and is the focus of further analysis in this paper. The model structure is depicted in Figures 4C, 5, and 6.

Further evidence of the presence of the overlayer of O atoms is provided by the data of the specular rod (Figure 2).

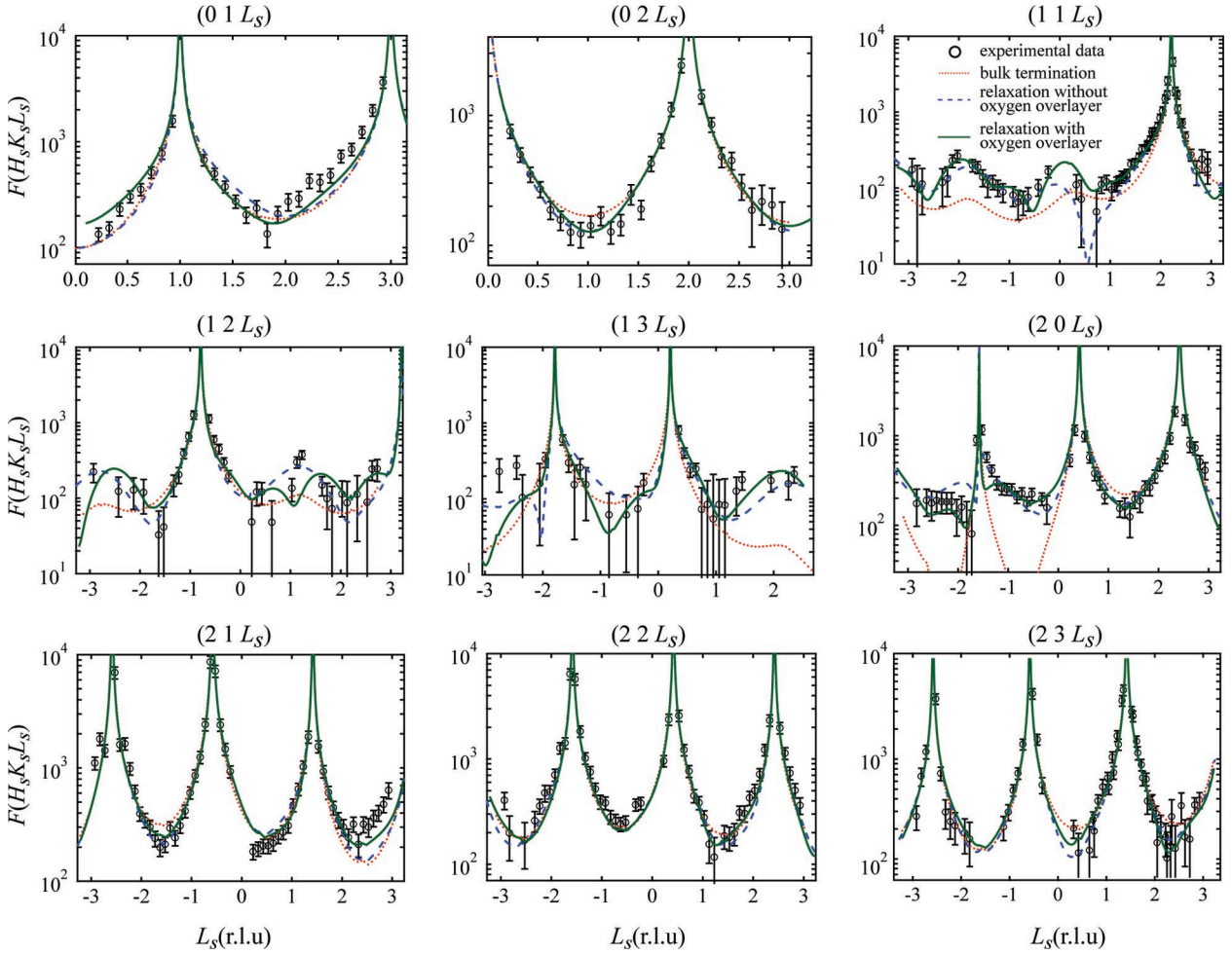

FIGURE 3. Measured structure factors of the (10$\bar{1}$4) surface of $MnCO_3$ in nonspecular geometries at 90% relative humidity and 295 K. The rods are identified in each panel. Lines show the calculated scattering based on the optimized models. The lines correspond to the same models described in the caption of Figure 2. Across the nine panels, there are a total of 385 data points (i.e., structure factors).

For L_s < 2 rlu (reciprocal-lattice units), corresponding to 2.2 Å^{-1}, the scattering is not sensitive to the molecular-scale structure of the interfacial water because the individual layers of the fluid structure are unresolved at this length scale (*8*). Therefore, the predicted scattering for models with and without an oxygen overlayer are nearly identical, as shown by the overlapping curves in Figure 2 for L_s < 2 rlu. For L_s > 2 rlu, however, molecular-scale water layers begin to resolve, and there is an improved fit by model no. 4 relative to the other models, which lack the overlay of O atoms.

In model no. 4, atoms in the surface region have both lateral and vertical relaxations in the first two layers (Table S1C). In the surface-normal direction, the Mn atoms in the first two layers remain undisplaced to within ± 0.01 Å whereas the CO_3 groups are displaced by −0.081 ± 0.024 Å (C_1) and −0.064 ± 0.021 Å (C_2) (*22*, *31*). The first-layer Mn atoms are displaced laterally by 0.041 ± 0.024 Å and 0.067 ± 0.012 Å in *x* and *y* respectively. The CO_3 groups are not displaced in *x* to within ± 0.035 Å but move 0.069 ± 0.031 Å in *y* (Table S1C and Figure 5C). The average bond length (Table 2) of the substrate-directed Mn−O bonds is 2.18 Å, which is comparable to the bulk value of 2.19 Å. The slightly shorter average bond length is consistent with the longer sixth Mn_1-O_w bond (2.59 Å). The first-layer CO_3 groups tilt by −4.2 ± 2.1° in *phi* (toward the surface plane) (Figure 4C and Table 1) and −2.6 ± 1.2° in *chi* (Table 1). The lateral positions of the O atoms in the overlayer are shifted by 0.157 ± 0.052 Å along the *x*-direction and 0.626 ± 0.029 Å along the *y*-direction compared to the first-layer Mn atoms (Figure 5A).

The overlayer of O atoms in model no. 4 is inferred as a hydration layer of OH or H_2O, although the H atoms cannot be tested for by our experimental method because of their weak X-ray scattering factor. The presence of a hydration layer is consistent with several studies on other materials. Yan et al. (*32*) show that approximately three water layers adsorb on alumina surfaces under typical atmospheric conditions (298 K and 50−60% RH). Eng et al. (*23*) suggest that there is a water layer on the relaxed (0001) surface of Al_2O_3 in the presence of water vapor. Al-Hosney and Grassian report that the number of water layers present on calcite depends on relative humidity (*14*). The number of water layers is not determined by the data constrains of our study (see further in §4.2). The term "hydration layer" in this paper therefore refers to the possibilities of a single OH layer or single or multiple H_2O layers.

4. Discussion

4.1 Bond-Valence Sums. The chemical plausibility of model no. 4 can be tested by calculating the bond-valence sums of atoms in the surface region. Bond valence (BV) is related to bond length *R*, as follows (*8*, *21*, *33*):

$$\mathrm{BV} = \exp((R_0 - R)/B) \qquad (2)$$

where R_0 and *B* are parameters specified for the two-atom combination forming the bond. The bond-valence sum (ΣBV) of an atom in the surface region is calculated by applying eq 2 to each neighboring atom that is separated by 2.60 Å or

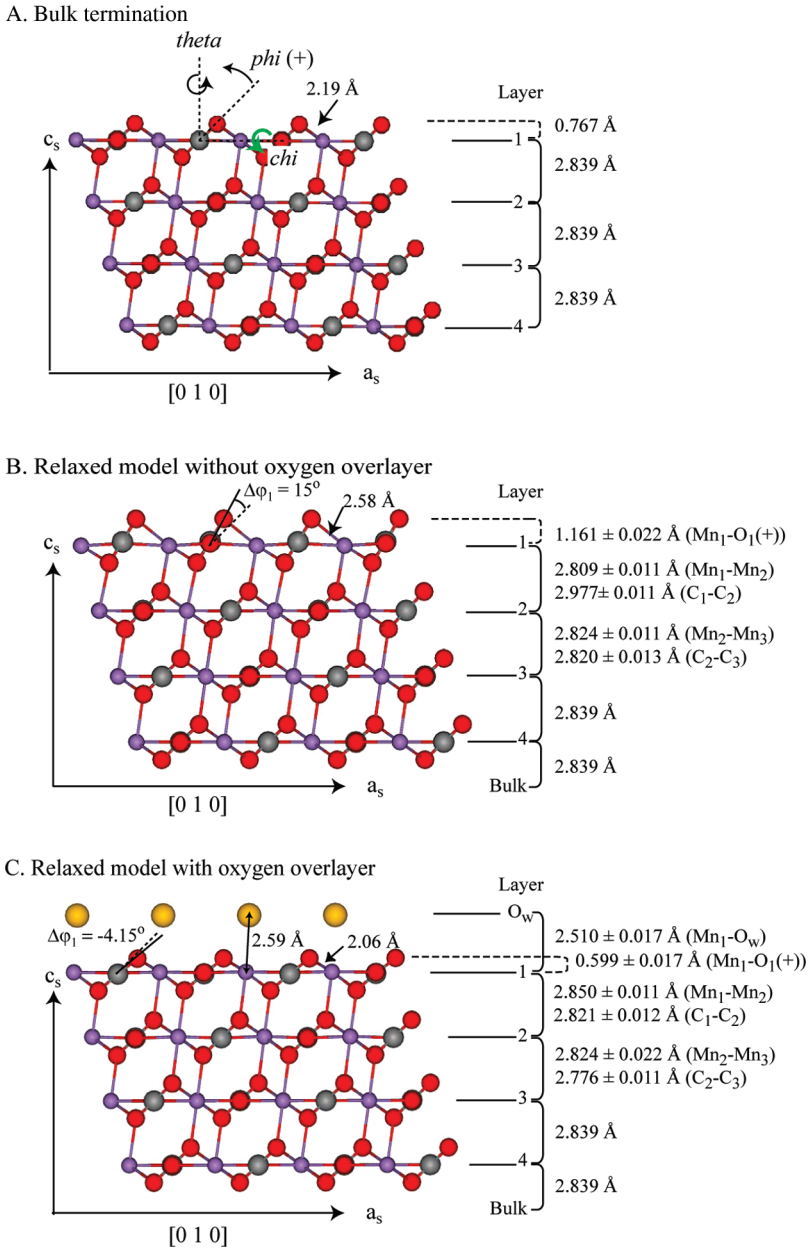

FIGURE 4. Atomic layer sequence and layer spacing of several optimized surface models. (A) Bulk termination (model no.1). (B) Relaxed structure without oxygen overlayer (model no. 3). (C) Relaxed structure with oxygen overlayer (model no. 4, i.e., best-fit model). Red, gray, and purple spheres indicate O, C, and Mn atoms, respectively. The yellow sphere indicates the O atom in the overlayer.

less, which is a distance sufficient to include all nearest neighbors, and further by summing the separate calculations. As a reference, the BV sums of Mn, O, and C are 2.00, 2.00, and 4.00 vu (valence units), respectively, within the bulk structure of $MnCO_3$. A BV sum of an atom in the surface region that is lower than the value in the bulk region is termed "undersaturated", a condition which implies either atomic undercoordination or atypically long bonds. Conversely, a BV sum greater than the reference value is termed "oversaturated" and indicates either atomic overcoordination or atypically short bonds.

The bond-valence sums of the models are given in Table S1. The BV sums are based upon the Mn−O bond lengths given in Table 2 (see labeling in Figure 6). In the unrelaxed, bulk-terminated model, the first-layer Mn and O atoms have BV sums of 1.70 and 1.66 vu, respectively, compared to the reference value of 2.00 in both cases. The atoms in this model are therefore undersaturated. The optimized model without an overlayer of oxygen leads to an increase in the average Mn−O bond length and therefore results in a BV sum of 1.56 ± 0.03 vu. The terminal O in the first-layer CO_3 is also undersaturated, having a BV sum of 1.43 ± 0.03 vu. The BV sums of these two models are much lower than the reference values and therefore suggest that the models are not chemically plausible.

The BV sums for the first-layer Mn and terminal O of the CO_3 group of the best-fit model are 1.92 ± 0.03 and 1.80 ± 0.03 vu, respectively. Therefore, the surface atoms are slightly undersaturated in the best-fit model. These Mn and O atoms are, however, still undersaturated by 0.08 and 0.20 vu, respectively. Bargar et al. report that a hydrogen bond (O:::H) contributes $0.13 \leq BV_{O:::H} \leq 0.25$ vu and that a single proton of a hydroxyl group (OH) contributes $0.68 \leq BV_{OH} \leq 0.88$ vu (*33*). Therefore, an additional disordered hydration layer lying above the partially ordered oxygen overlayer could provide hydrogen bonding that reduces the undersaturation of the oxygen compared to the calculated value.

A. Lateral displacements (a_s vs. b_s) of oxygen atoms in the hydration layer

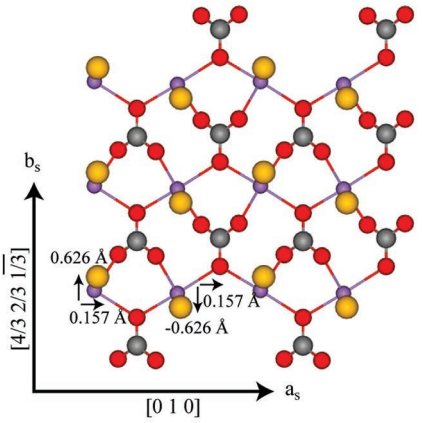

B. Lateral displacements (b_s vs. c_s) of surface atoms

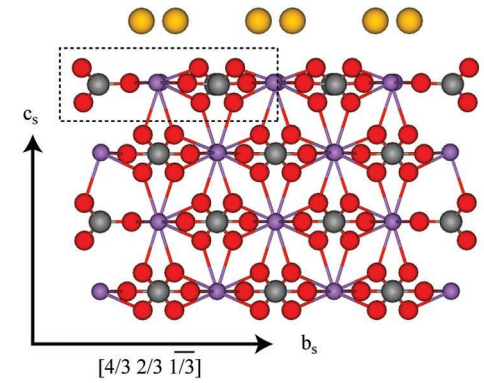

C. Enlarged view of manganese and carbon displacements (boxed region in B)

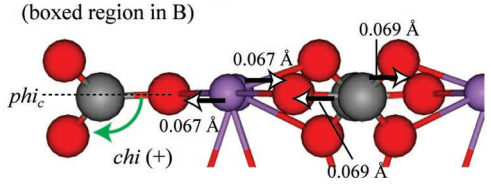

FIGURE 5. Best-fit model of the three-dimensional relaxed $MnCO_3$ structure with an oxygen overlayer. (A) a_s-b_s view. (B) b_s-c_s view. (C) Enlarged view of panel B. Red, gray, and purple spheres indicate O, C, and Mn atoms, respectively. The yellow sphere indicates the O atom in the overlayer. (The c_s-a_s view is shown in Figure 4C.)

TABLE 1. Comparison of Rotation Angles (Figure 4A) of Carbonates in the Optimized Models Without and With an Oxygen Overlayer

		rotation angles	
layer	rotation axes of carbonate group	relaxed surface without oxygen overlayer	relaxed surface with oxygen overlayer
1	*Phi* (φ)	15.0° ± 2.5	−4.2° ± 2.1
	Chi (χ)	3.3° ± 0.2	−2.6° ± 1.2
	Theta (θ)	0°	0°
2	*Phi* (φ)	2.9° ± 1.7	0.2° ± 1.5
	Chi (χ)	1.0° ± 0.9	0.5° ± 1.0
	Theta (θ)	0°	0°

4.2 Hydration Layer. The determined Mn_1-O_w bond length is 2.59 ± 0.04 Å, a value which is consistent with the bonding of the water oxygen to a surface Mn atom (e.g., $Mn-OH_2$). Furthermore, the occupancies of oxygen overlayer (O_w) and manganese are both 0.84 within error, implying coordinative bonding between these atoms. The Debye−Waller factor of the O atoms in the overlayer (O_w) is 2.04 ± 1.71 Å^2 (Table S1C), compared to a bulk oxygen value of 0.57 Å^2. These increased Debye−Waller factor values imply high thermal and/or static disorder for the O atoms, as expected for water overlayer.

TABLE 2. Comparison of Mn−O Bond Lengths in the First Layer of the Optimized Models Without and With an Oxygen Overlayer

Mn−O bond	bulk termination (Å)	relaxed surface without oxygen overlayer (Å)	relaxed surface with oxygen overlayer (Å)
1: $Mn_1-O_1(+)$	2.19	2.58	2.06
2: Mn_1-O_1	2.19	2.17	2.30
3: Mn_1-O_1	2.19	2.28	2.15
4: $Mn_1-O_1(-)$	2.19	2.10	2.13
5: $Mn_1-O_2(+)$	2.19	2.14	2.25
average bond length	2.19	2.25	2.18

The best-fit model we derive for the hydration of the $(10\bar{1}4)$ surface of $MnCO_3$ can be compared to that reported by Geissbühler et al. (*19*) for $CaCO_3$, which is isostructural to $MnCO_3$. The nearest O atoms in the overlayer on $CaCO_3$ are displaced in the *x*-direction by 0.62 ± 0.08 Å and in the *y*-direction by 1.78 ± 0.08 Å relative to the positions of in-plane Ca. These lateral displacements are approximately three times larger than their respective counterparts for our best-fit model of the surface region of $MnCO_3$. The Ca_1-O_{w1} bond length is 2.97 ± 0.12 Å, representing a 29% increase over the length in the bulk region of $CaCO_3$ (2.3 Å) (*19*). For comparison, the bond length increases by 19% in the case of $MnCO_3$. A lower affinity for the electrons of the oxygen atom of water by Ca than for Mn, as reflected by the lower electron negativity of Ca (1.00 on the Pauling scale) than that of Mn (1.55), might contribute to the explanation for the structural differences in the best-fit models (*34*).

Compared to our best-fit model having a single overlayer of oxygen, Geissbühler et al. (*19*) obtain an improved model fit (having a further 30% reduction in χ^2) by including a second overlayer of oxygen. In that work, the oxygen layers are located at 2.3 ± 0.1 Å and 3.5 ± 0.2 Å above the surface. In our work, the calculated structure factors of a model having a second overlayer of oxygen are identical within experimental error to those of the best-fit model having a single overlayer of oxygen. Therefore, we are not able to uniquely resolve a possible second overlayer. Nonspecular crystal truncation rods, as mainly employed in this study, are sensitive only to

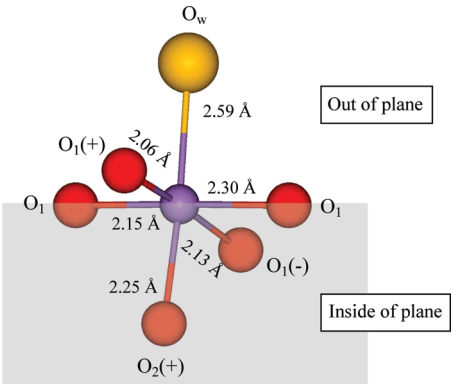

FIGURE 6. Mn−O bond of the first layer of the $(10\bar{1}4)$ $MnCO_3$ surface in the best-fit model (Figure 5). Red and purple spheres indicate first-layer O and Mn atoms, respectively. The yellow sphere indicates the O atom in the overlayer.

the water molecules ordered with respect to the atomic structure of $MnCO_3$ surfaces. Further analysis regarding possible disordered water layers is therefore not pursued in this study.

4.3 Environmental Implications. The best-fit model for interpreting the CTR scattering data of the hydrated $(10\bar{1}4)$ surface of $MnCO_3$ includes an overlayer of oxygen. The significant improvement in the BV sum for Mn_1 by incorporating an overlayer of oxygen in the model suggests that relaxation is driven by the initial undercoordination of the first-layer Mn atoms (cf. the bulk-terminated model). This conclusion is further supported by the atomic occupancies of the best-fit model showing that Mn singly coordinates with O_w. In contrast, the shortest $O_{CO_3}-O_w$ distance is 3.22 Å, which is large enough to conclude that the hydrogen atoms associated with O_w do not bond strongly to O_{CO_3}. O_w and O_{CO_3} may, however, interact through bonding with additional water layers, as suggested by the undersaturation of 0.20 vu for O_{CO_3} (*35*).

The interaction of mineral surfaces with water is central to many natural processes, such as dissolution, precipitation, and metal and ligand sorption (*23*, *33*, *36*, *37*). In particular, the hydration layer can affect the reactivity of the mineral surface by altering the surface structure and thereby affecting the equilibrium binding constants of protons and heavy metal ions to the mineral surface (*22*). The hydration of minerals further affects the chemical reactivity of atmospheric dust particles toward pollutants such as NO_x and SO_x (*14*, *38*). The water−mineral interface also regulates many industrial processes, including electrode operation, preparation of catalysts, and fabrication of ultra-clean semiconductor surfaces (*39*). Accurate structural models of the mineral−water interface should lead both to improved understanding and better quantitative predictions in these numerous applications.

Acknowledgments

S.T.M. acknowledges support received from the Chemical Sciences, Geosciences, and Biosciences Division of the Office of Basic Energy Sciences in the U.S. Department of Energy. P.J.E. and T.P.T. acknowledge support of the National Science Foundation. Use of GeoSoilEnviroCARS was supported by NSF Earth Sciences, DOE Geosciences, the State of Illinois, and the W. M. Keck Foundation. Use of the Advance Photon Source was supported by DOE-Basic Energy Sciences. Minerals were obtained from the collections of the Harvard University Mineralogical Museum. We thank Cynthia Friend and Matthew Newville for valuable discussion and advice.

Supporting Information Available

Table S1: Fractional coordinates, Debye−Waller factors, occupancies, and bond-valence sums of the optimized models. Figure S1: AFM micrograph of a freshly cleaved surface of $MnCO_3$. Figure S2: A section of reciprocal space plotted in the surface-indexed coordinate system. Appendix S1: Surface indexing and the Bragg condition. Appendix S2: Basic theory for analysis by crystal truncation rods. This material is available free of charge via the Internet at http://pubs.acs.org.

Literature Cited

(1) Sternbeck, J. Kinetics of rhodochrosite crystal growth at 25°C: the role of surface speciation. *Geochim. Cosmochim. Acta* **1997**, *61*, 785−793.

(2) Jensen, D. L.; Boddum, J. K.; Tjell, J. C.; Christensen, T. H. The solubility of rhodochrosite ($MnCO_3$) and siderite ($FeCO_3$) in anaerobic aquatic environments. *Appl. Geochem.* **2002**, *17*, 503−511.

(3) Jun, Y. S.; Kendall, T. A.; Martin, S. T.; Friend, C. M.; Vlassak, J. J. Heteroepitaxial nucleation and oriented growth of manganese oxide islands on carbonate minerals under aqueous conditions. *Environ. Sci. Technol.* **2005**, *39*, 1239−1249.

(4) Glasby, G. P.; Schulz, H. D. E_H, pH Diagrams for Mn, Fe, Co, Ni, Cu and As under seawater conditions: Application of two new types of E_H, pH diagrams to the study of specific problems in marine geochemistry. *Aquat. Geochem.* **1999**, *5*, 227−248.

(5) Bluhm, H.; Inoue, T.; Salmeron, M. Formation of dipole-oriented water films on mica substrates at ambient conditions. *Surf. Sci.* **2000**, *462*, L599−L602.

(6) Hu, J.; Xiao, X. D.; Ogletree, D. F.; Salmeron, M. The structure of molecularly thin films of water on mica in humid environments. *Surf. Sci.* **1995**, *344*, 221−236.

(7) de Leeuw, N. H.; Parker, S. C. Atomistic simulation of the effect of molecular adsorption of water on the surface structure and energies of calcite surfaces. *J. Chem. Soc. Faraday Trans.* **1997**, *93*, 467−475.

(8) Fenter, P.; Sturchio, N. C. Mineral-water interfacial structures revealed by synchrotron X-ray scattering. *Prog. Surf. Sci.* **2004**, *77*, 171−258.

(9) Liu, P.; Kendelewicz, T.; Brown, G. E.; Nelson, E. J.; Chambers, S. A. Reaction of water vapor with alpha-Al_2O_3(0001) and alpha-Fe_2O_3(0001) surfaces: synchrotron X-ray photoemission studies and thermodynamic calculations. *Surf. Sci.* **1998**, *417*, 53−65.

(10) Kerisit, S.; Parker, S. C. Free energy of adsorption of water and metal ions on the {1014} calcite surface. *J. Am. Chem. Soc.* **2004**, *126*, 10152−10161.

(11) Stipp, S. L.; Hochella, M. F., Jr. Structure and bonding environments at the calcite surface as observed with X-ray photoelectron spectroscopy (XPS) and low energy electron diffraction (LEED). *Geochim. Cosmochim. Acta* **1991**, *55*, 1723−1736.

(12) Davis, J. A.; Fuller, C. C.; Cook, A. D. A model for trace metal sorption processes at the calcite surface: Adsorption of Cd^{2+} and subsequent solid solution formation. *Geochim. Cosmochim. Acta* **1987**, *51*, 1477−1490.

(13) Masel, R. I. *Principles of Adsorption and Reaction on Solid Surfaces*; Wiley: New York, 1996.

(14) Al-Hosney, H. A.; Grassian, V. H. Water, sulfur dioxide and nitric acid adsorption on calcium carbonate: A transmission and ATR-FTIR study. *Phys. Chem. Chem. Phys.* **2005**, *7*, 1266−1276.

(15) Robinson, I. K.; Tweet, D. J. Surface x-ray diffraction. *Rep. Prog. Phys.* **1992**, *55*, 599−651.

(16) Fenter, P. A. X-ray reflectivity as a probe of mineral-fluid interfaces: A user guide. *Rev. Mineral. Geochem.* **2002**, *49*, 149−220.

(17) Feidenhansl, R. Surface-structure determination by x-ray-diffraction. *Surf. Sci. Rep.* **1989**, *10*, 105−188.

(18) Fenter, P.; Geissbuhler, P.; DiMasi, E.; Srajer, G.; Sorensen, L. B.; Sturchio, N. C. Surface speciation of calcite observed in situ by high-resolution X-ray reflectivity. *Geochim. Cosmochim. Acta* **2000**, *64*, 1221−1228.

(19) Geissbuhler, P.; Fenter, P.; DiMasi, E.; Srajer, G.; Sorensen, L. B.; Sturchio, N. C. Three-dimensional structure of the calcite-water interface by surface X-ray scattering. *Surf. Sci.* **2004**, *573*, 191−203.

(20) Robinson, I. K. Crystal truncation rods and surface roughness. *Phys. Rev. B* **1986**, *33*, 3830−3836.

(21) Trainor, T. P.; Eng, P. J.; Brown, G. E.; Robinson, I. K.; De Santis, M. Crystal truncation rod diffraction study of the alpha-Al_2O_3 (1(1)over-bar-0 2) surface. *Surf. Sci.* **2002**, *496*, 238−250.

(22) Trainor, T. P.; Chaka, A. M.; Eng, P. J.; Newville, M.; Waychunas, G. A.; Catalano, J. G.; Brown, G. E. Structure and reactivity of the hydrated hematite (0001) surface. *Surf. Sci.* **2004**, *573*, 204−224.

(23) Eng, P. J.; Trainor, T. P.; Brown, G. E.; Waychunas, G. A.; Newville, M.; Sutton, S. R.; Rivers, M. L. Structure of the hydrated alpha-Al_2O_3 (0001) surface. *Science* **2000**, *288*, 1029−1033.

(24) Duckworth, O. W.; Martin, S. T. Dissolution rates and pit morphologies of rhombohedral carbonate minerals. *Am. Mineral.* **2004**, *89*, 554−563.

(25) Jun, Y. S.; Martin, S. T. Microscopic observations of reductive manganite dissolution under oxic conditions. *Environ. Sci. Technol.* **2003**, *37*, 2363−2370.

(26) Effenberger, H.; Mereiter, K.; Zemann, J. Crystal-structure refinements of magnesite, calcite, rhodochrosite, siderite, smithonite, and dolomite, with discussion of some aspects of the stereochemistry of calcite type carbonates. *Z. Kristallogr.* **1981**, *156*, 233−243.

(27) Trainor, T. P.; Eng, P. J.; Robinson, I. K. Calculation of crystal truncation rod structure factors for arbitrary rational surface terminations. *J. Appl. Crystallogr.* **2002**, *35*, 696−701.

(28) Brown, G. S.; Moncton, D. E. *Handbook on Synchrotron Radiation*; Elsevier Science: Amsterdam, 1991.
(29) Vlieg, E. ROD: A program for surface X-ray crystallography. *J. Appl. Crystallogr.* **2000**, *33*, 401−405.
(30) Hamilton, W. C. Significance tests on crystallographic R factor. *Acta Crystallogr.* **1965**, *18*, 502−510.
(31) Shluger, A. L.; Kantorovich, L. N.; Livshits, A. I.; Gillan, M. J. Ionic and electronic processes at ionic surfaces induced by atomic-force-microscope tips. *Phys. Rev. B* **1997**, *56*, 15332−15344.
(32) Yan, B. D.; Meilink, S. L.; Warren, G. W.; Wynblatt, P. Water-adsorption and surface conductivity measurements on alpha-alumina substrates. *IEEE Trans. Compon. Hybr.* **1987**, *10*, 247−251.
(33) Bargar, J.; Towle, S. N.; Brown, G. E.; Parks, G. A. XAFS and bond-valence determination of the structures and compositions of surface functional groups and Pb(II) and Co(II) sorption products on single-crystal α-Al_2O_3. *J. Colloid Interface Sci.* **1997**, *185*, 473−492.
(34) Lide, D. R. *CRC Handbook of Chemistry and Physics*; CRC Press: New York, 1997.
(35) Hiemstra, T.; Yong, H.; Van Riemsdijk, W. H. Interfacial charging phenomena of aluminum (hydr)oxides. *Langmuir* **1999**, *15*, 5942−5955.
(36) Brown, G. E. How minerals react with water. *Science* **2001**, *294*, 67−70.
(37) Fenter, P.; Sturchio, N. C. Structure and growth of stearate monolayers on calcite: First results of an in situ X-ray reflectivity study. *Geochim. Cosmochim. Acta* **1999**, *63*, 3145−3152.
(38) Al-Abadleh, H. A.; Al-Hosney, H. A.; Grassian, V. H. Oxide and carbonate surfaces as environmental interfaces: the importance of water in surface composition and surface reactivity. *J. Mol. Catal. A, Chem.* **2005**, *228*, 47−54.
(39) Johnson, M. A.; Stefanovich, E. V.; Truong, T. N.; Gunster, J.; Goodman, D. W. Dissociation of water at the MgO(100)-water Interface: Comparison of theory with experiment. *J. Phys. Chem. B* **1999**, *103*, 3391−3398.

Received for review September 12, 2006. Revised manuscript received March 14, 2007. Accepted March 19, 2007.

ES062171V

Structure of the Hydrated ($10\bar{1}4$) Surface of Rhodochrosite ($MnCO_3$)

Young-Shin Jun, Sanjit K. Ghose, Thomas P. Trainor,
Peter J. Eng, and Scot T. Martin

Supporting Information:

10 Pages

1 Table

2 Figure

2 Appendices

		(A) Bulk termination				(B) Relaxed surface without an oxygen overlayer						
Layer		**x**	**y**	**z**	**ΣBV**	**X**	**y**	**z**	**Δz [Å]**	**DW [Å^2]**	**Occ**	**ΣBV**
1	O_1(+)	0.752	-0.135	0.635	1.66	0.707(4)	-0.14(1)	0.697(5)	0.35(3)	0.57	0.83(4)	1.43(3)
1	O_1(+)	0.252	1.135	0.635	1.66	0.207(4)	1.14(1)	0.697(5)	0.35(3)	0.57	0.83(4)	1.43(3)
1	Mn_1	0.395	0.500	0.500	1.70	0.394(3)	0.516(2)	0.492(2)	-0.05(1)	0.51	0.85(4)	1.56(3)
1	Mn_1	0.895	0.500	0.500	1.70	0.894(3)	0.484(2)	0.492(2)	-0.05(1)	0.51	0.85(4)	1.56(3)
1	C_1	0.645	0.000	0.500	3.97	0.630(4)	-0.01(1)	0.523(5)	0.13(3)	0.48	0.83(4)	3.97(3)
1	C_1	0.145	1.000	0.500	3.97	0.130(4)	1.01(1)	0.523(5)	0.13(3)	0.48	0.83(4)	3.97(3)
1	O_1	0.645	0.270	0.500	2.00	0.630(4)	0.26(1)	0.510(5)	0.06(3)	0.57	0.83(4)	1.94(3)
1	O_1	0.145	0.730	0.500	2.00	0.130(4)	0.74(1)	0.510(5)	0.06(3)	0.57	0.83(4)	1.94(3)
1	O_1(-)	0.539	-0.135	0.365	2.01	0.553(4)	-0.16(1)	0.363(5)	-0.01(3)	0.57	0.83(4)	2.07(3)
1	O_1(-)	0.039	1.135	0.365	2.01	0.053(4)	1.16(1)	0.363(5)	-0.01(3)	0.57	0.83(4)	2.07(3)
2	O_2(+)	0.857	0.635	0.135	2.00	0.848(4)	0.635(4)	0.143(4)	0.05(2)	0.57	1.00	2.00(3)
2	O_2(+)	0.357	0.365	0.135	2.00	0.348(4)	0.365(4)	0.143(4)	0.05(2)	0.57	1.00	2.00(3)
2	Mn_2	0.500	1.000	0.000	2.04	0.497(2)	0.996(2)	-0.003(2)	-0.02(1)	0.51	1.00	1.95(3)
2	Mn_2	0.000	0.000	0.000	2.04	-0.003(2)	0.004(2)	-0.003(2)	-0.02(1)	0.51	1.00	1.95(3)
2	C_2	0.250	0.500	0.000	3.96	0.246(4)	0.497(4)	-0.001(4)	-0.01(2)	0.48	1.00	3.96(3)
2	C_2	0.750	0.500	0.000	3.96	0.746(4)	0.503(4)	-0.001(4)	-0.01(2)	0.48	1.00	3.96(3)
2	O_2	0.250	0.770	0.000	2.00	0.246(4)	0.767(4)	-0.006(4)	-0.03(2)	0.57	1.00	1.98(3)
2	O_2	0.750	0.230	0.000	2.00	0.746(4)	0.233(4)	-0.006(4)	-0.03(2)	0.57	1.00	1.98(3)
2	O_2(-)	0.143	0.365	-0.135	2.00	0.145(4)	0.358(4)	-0.141(4)	-0.03(2)	0.57	1.00	2.04(3)
2	O_2(-)	0.643	0.635	-0.135	2.00	0.645(4)	0.642(4)	-0.141(4)	-0.03(2)	0.57	1.00	2.04(3)
(A) Bulk termination						**(C) Relaxed surface with an oxygen overlayer**						
w	O_w	-	-	-	-	0.91(1)	0.36(1)	0.941(9)	-	2.04	0.84(10)	-
w	O_w	-	-	-	-	0.41(1)	0.65(1)	0.941(9)	-	2.04	0.84(10)	-
1	O_1(+)	0.752	-0.135	0.635	1.66	0.76(1)	-0.16(1)	0.60(2)	-0.20(1)	0.57	0.94(5)	1.80(3)
1	O_1(+)	0.252	1.135	0.635	1.66	0.26(1)	1.16(1)	0.60(2)	-0.20(1)	0.57	0.94(5)	1.80(3)
1	Mn_1	0.395	0.500	0.500	1.70	0.390(3)	0.514(2)	0.499(2)	0.00(1)	0.51	0.84(4)	1.92(3)
1	Mn_1	0.895	0.500	0.500	1.70	0.890(3)	0.486(2)	0.499(2)	0.00(1)	0.51	0.84(4)	1.92(3)
1	C_1	0.645	0.000	0.500	3.97	0.646(5)	-0.014(6)	0.486(4)	-0.08(2)	0.48	0.94(5)	3.97(3)
1	C_1	0.145	1.000	0.500	3.97	0.146(5)	1.014(6)	0.486(4)	-0.08(2)	0.48	0.94(5)	3.97(3)
1	O_1	0.645	0.270	0.500	2.00	0.646(9)	0.26(1)	0.50(1)	-0.02(7)	0.57	0.94(5)	1.95(3)
1	O_1	0.145	0.730	0.500	2.00	0.146(9)	0.74(1)	0.50(1)	-0.02(7)	0.57	0.94(5)	1.95(3)
1	O_1(-)	0.539	-0.135	0.365	2.01	0.53(1)	-0.14(1)	0.36(1)	-0.05(6)	0.57	0.94(5)	2.11(3)
1	O_1(-)	0.039	1.135	0.365	2.01	0.03(1)	1.14(1)	0.36(1)	-0.05(6)	0.57	0.94(5)	2.11(3)
2	O_2(+)	0.857	0.635	0.135	2.00	0.853(4)	0.633(4)	0.125(4)	-0.06(2)	0.57	1.00	1.92(3)
2	O_2(+)	0.357	0.365	0.135	2.00	0.353(4)	0.367(4)	0.125(4)	-0.06(2)	0.57	1.00	1.92(3)
2	Mn_2	0.500	1.000	0.000	2.04	0.496(2)	0.992(2)	-0.003(2)	-0.01(1)	0.51	1.00	2.07(3)
2	Mn_2	0.000	0.000	0.000	2.04	-0.004(2)	0.008(2)	-0.003(2)	-0.01(1)	0.51	1.00	2.07(3)
2	C_2	0.250	0.500	0.000	3.96	0.247(4)	0.500(4)	-0.011(4)	-0.06(2)	0.48	1.00	3.96(3)
2	C_2	0.750	0.500	0.000	3.96	0.747(4)	0.500(4)	-0.011(4)	-0.06(2)	0.48	1.00	3.96(3)
2	O_2	0.250	0.770	0.000	2.00	0.247(4)	0.770(4)	-0.013(4)	-0.08(2)	0.57	1.00	2.00(3)
2	O_2	0.750	0.230	0.000	2.00	0.747(4)	0.230(4)	-0.013(4)	-0.08(2)	0.57	1.00	2.00(3)
2	O_2(-)	0.143	0.365	-0.135	2.00	0.140(4)	0.364(4)	-0.146(4)	-0.06(2)	0.57	1.00	2.07(3)
2	O_2(-)	0.643	0.635	-0.135	2.00	0.640(4)	0.636(4)	-0.146(4)	-0.06(2)	0.57	1.00	2.07(3)

Table S1

Table S1. (A) Fractional *x*-*y*-*z* coordinates and bond-valence sums (ΣBV) of atoms in the surface model for a bulk termination and (B, C) fractional coordinates, Debye-Waller factors (DW), occupancies (Occ), and bond-valence sums of the optimized models without and with an oxygen overlayer. The cell parameters are $|\mathbf{a}_s|$ = 7.581 Å, $|\mathbf{b}_s|$ = 4.768 Å, $|\mathbf{c}_s|$ = 5.678 Å, and $\alpha = \beta = \gamma = 90^{\circ}$. The Δz values (expressed in Å) are the changes in the *z*-positioning of the layers with respect to the bulk termination. Subscript numbers indicate the layer where the atoms reside. Signs (+) and (-) correspond to higher and lower *z*-positions of oxygen compared to carbon in the same carbonate (see Figure 4). Estimated errors from the fit at the 95% confidence level are given in parentheses. Values without reported errors were fixed in the fit or the errors are several magnitudes smaller than the calculated values. The error values are applied to the last digit of the calculated values (e.g., 0.707(4) = 0.707 ± 0.004).

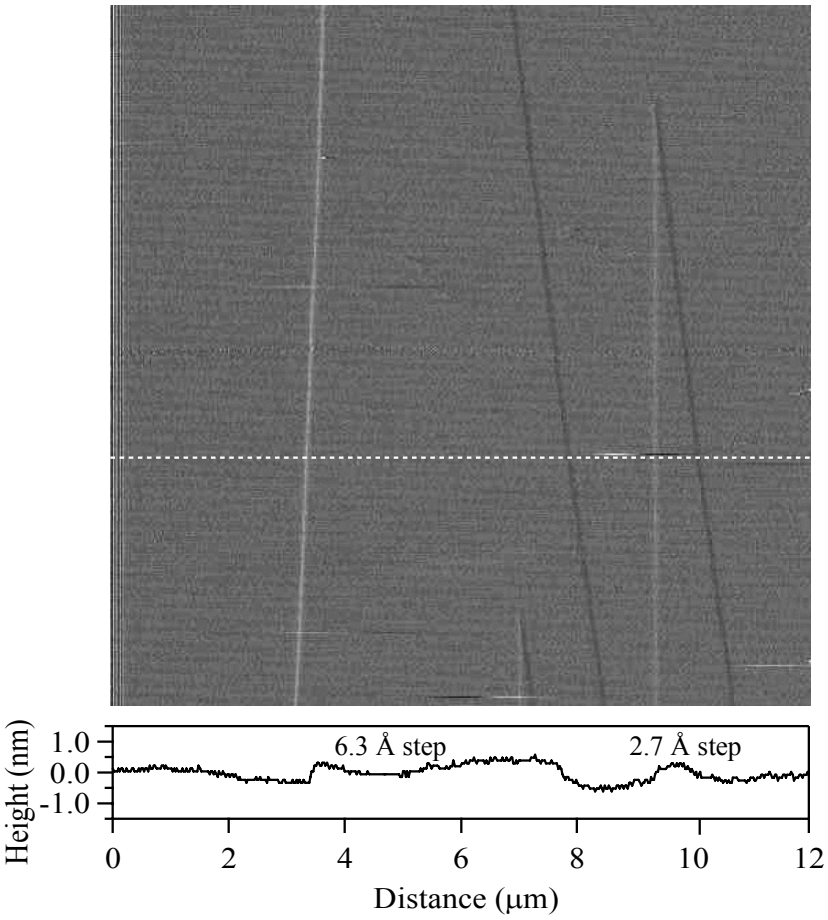

Figure S1. AFM micrograph of a freshly cleaved surface of $MnCO_3$. The micrograph is shown in deflection mode (12 × 12 μm^2) during exposure at 295 K to a solution having pH = 6.4. The height cross section corresponds to the white dotted line in the micrograph. Except for the presence of several steps, the surface terrace is smooth. There is low surface roughness on the individual terraces. The waviness of AFM image is the artifact from the instrument. From the least-squares CTR analysis, a root-mean-square roughness of 1.39 ± 0.45 Å is determined, which is consistent with the AFM observations of a large terrace morphology, with roughness of individual terraces on the order of a few angstroms (essentially at the noise floor of the instrument). The measurements are taken from the central areas of the test structures in order to avoid edge effects.

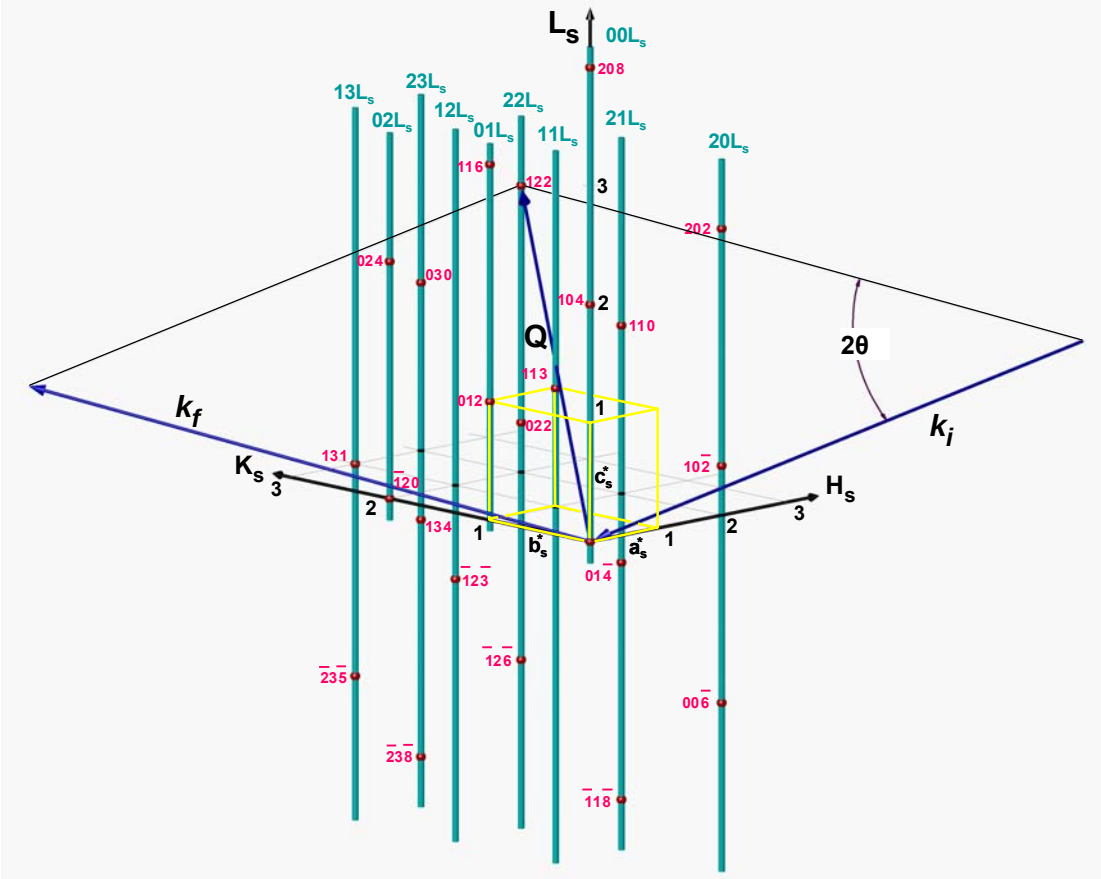

Figure S2. A section of reciprocal space plotted in the surface-indexed coordinate system. The values of H_s, K_s, and L_s along the three perpendicular axes respectively correspond to the vectors $\mathbf{a}^*_s$, $\mathbf{b}^*_s$, and $\mathbf{c}^*_s$ of the $(10\bar{1}4)$-surface reciprocal lattice of $MnCO_3$ (shown in yellow). Values are expressed as reciprocal-lattice units (r.l.u.). Light blue vertical lines (called rods) show sweeps in reciprocal space along the ten measured CTRs. A position along one of these lines corresponds to the L_s-axes of Figures 2 and 3. Red dots, which are labeled using bulk indexing, show the H_s-K_s-L_s positions corresponding to the Bragg peaks of the bulk crystal. The shown wavevectors $\boldsymbol{k_i}$ and $\boldsymbol{k_f}$ of incident and scattered radiation illustrate the geometry satisfying the diffraction condition for the (122) Bragg peak (i.e., momentum transfer $\boldsymbol{Q}$ given by $\boldsymbol{k_i} - \boldsymbol{k_f}$ terminates at the (122) position). The CTRs are perpendicular to the H_s-K_s plane.

Appendix S1. Surface indexing and the Bragg condition

The periodicity of an infinite crystal can be fully represented by a complete set of reciprocal-lattice vectors $\boldsymbol{G_{HKL}}$. These vectors, which are normal to the atomic planes of the crystal, have lengths equal to the reciprocal of the interplanar spacing. The labels *H, K,* and *L* correspond to the Miller indices of the atomic planes (*l*). The reciprocal-space representation of the three-dimensional periodicity of the $MnCO_3$ crystal is shown in Figure S2 by the red dots, which correspond to the terminations of the set of $\boldsymbol{G_{HKL}}$ vectors drawn from the origin.

Figure S2 also shows a surface-indexing coordinate system for the $(10\bar{1}4)$ termination of $MnCO_3$ crystal structure. A unit cell is constructed with orthogonal axes $\mathbf{a_s}$-$\mathbf{b_s}$-$\mathbf{c_s}$ such that the $\mathbf{a_s}$- and $\mathbf{b_s}$-axes lie in-plane with the surface and the $\mathbf{c_s}$ axis is normal to the surface. The corresponding axes of reciprocal space are denoted by $\mathbf{a}^*_s$-$\mathbf{b}^*_s$-$\mathbf{c}^*_s$ and for the case presented here have the relationship $a^*_s = 2\pi/a_s$ and so on. The axis H_s-K_s-L_s are the indices of reciprocal lattice vectors, where $\mathbf{a}^*_s$, $\mathbf{b}^*_s$ and $\mathbf{c}^*_s$ are the basis set defining the coordinate system.

The incident and the scattered x-ray beams are represented in Figure S2 by wavevectors, which are labeled $\boldsymbol{k_i}$ and $\boldsymbol{k_f}$, respectively. The wavevectors specify the beam direction and the reciprocal of the x-ray wavelength. For our elastic scattering experiment, the magnitudes of $\boldsymbol{k_i}$ and $\boldsymbol{k_f}$ are equal. For constructive interference of the incoming and the outgoing radiation, the momentum-transfer vector $\boldsymbol{Q}$, defined as $\boldsymbol{Q} = \boldsymbol{k}_f - \boldsymbol{k}_i = 2\pi(H_s\mathbf{a}^*_s + K_s\mathbf{b}^*_s + L_s\mathbf{c}^*_s)$, must coincide with one of the reciprocal-lattice vectors $\boldsymbol{G_{HKL}}$, thus defining the Bragg condition. As an example, Figure S2 shows the wavevectors $\boldsymbol{k_f}$ and $\boldsymbol{k_i}$ satisfying this condition for the (122) Bragg reflection.

Appendix S2. Basic theory for analysis by crystal-truncation rods

To introduce the concept of scattering along crystal-truncation rods, we first recall that the classic explanation of x-ray scattering from a crystalline material describes scattering intensity as confined in reciprocal space to multiple, finite, and approximately spherically bounded regions. These regions are compact, contain most of the scattered x-ray intensity, and are centered at the reciprocal-lattice points (also known as Bragg points and denoted by the red dots in Figure S2). Among other factors, the exact shapes of these bounded regions depend on the quality, the shape, and the size of the physical crystal. Of particular interest to our presentation is that an inverse relation exists between the crystal size (i.e., three-dimensional truncation) and the size of the bounded region. This effect occurs because of the truncation of infinite periodicity of a crystal by its physical surfaces. In the case of three-dimensional truncation, therefore, finite-size broadening induces a significant expansion of the bounded region for sufficiently small crystals. For typical measurements, for which the crystal size is greater than a few microns, the broadening is negligible compared to the instrument resolution, and the scattering by the crystal effectively approaches the infinite-size limit.

Having considered the case of three-dimensional truncation, we can next consider the case of one-dimensional truncation. Notably, our study conditions correspond to one-dimensional truncation because a large $MnCO_3$ crystal (ca. 3 mm × 3 mm) having an exposed $(10\bar{1}4)$ surface is irradiated by an x-ray beam having a cross section of 200 μm × 1000 μm.

Perturbations to the idealized, spherically bounded regions centered at the Bragg points occur when the model of an infinite crystal is replaced by one having one-

dimensional truncation (i.e., a surface). The surface interrupts the periodicity and therefore complete destructive interference in one direction (i.e., the surface-normal direction). The surface truncation thereby causes systematic changes in the angular distribution of the scattered x-ray intensity. These changes map into reciprocal space as bounded tails extending from the spherically bounded regions that are parallel to the surface normal (*2*). The tails, which are narrow in the H_s-K_s direction because of the nearly infinite extent of the crystal in the two non-truncated directions, join Bragg reflections along the L_s direction. The resulting object in reciprocal space is called a crystal-truncation rod (*3,4*) (e.g., a light blue vertical line in Figure S2).

The scattered x-ray intensity along the CTRs is the fundamental data employed in this study (see Figures 2 and 3). The intensity along CTRs is typically eight orders of magnitude lower than that occurring for bulk Bragg peaks because the scattering arises from just the approximately 10^{15} surface-region atoms located within the beam footprint. The high brilliance of synchrotron sources allows this much smaller amount of scattering to be investigated. The scattering intensity along CTRs is sensitive to the alternation of atomic positions in the near surface region compared to those in the bulk (*5*). Moreover, some rods are more selective than others to specific atoms and to specific vertical or lateral changes in positions. The ten CTRs corresponding to the data shown in Figures 2 and 3 are illustrated by the light blue lines in Figure S2.

In the surface-indexing system, rods are at integer H_s and K_s coordinates (light blue labels in Figure S2) and are continuous in the L_s direction (*6*). The position along one CTR corresponds to a position along an L_s-axis of Figures 2 and 3. The $(00L_s)$ rod is observed using specular scattering geometry with respect to the $(10\bar{1}4)$ surface, for

which the incident and the scattered beams are at equal angles to the physical surface of the cleaved crystal. The other rods in Figure S2 are observed by employing nonspecular geometries, where the incident and the scattered beams define a plane that is not perpendicular to the physical surface.

The scattering intensity along a CTR is proportional to $|F_T|^2$, where F_T is the calculated structure factor for a truncated crystal. The complex number F_T, which defines both intensity and phase, is calculated as follows (*6*):

$$F_T = S\rho\left(F_b F_{CTR} + \sum_{j=1}^{m} f_j \exp(i\mathbf{Q}\cdot\mathbf{r}_j)\exp[-\tfrac{1}{2}(|\mathbf{Q}|u_j)^2]\right) \quad \text{(S1)}$$

where S is an overall scale factor for the instrumentation, ρ is the surface roughness factor (*2*), F_b is the bulk structure factor, and $F_{CTR} = 1/[1-\exp(-i2\pi L_s)]$. The summation is over all atoms m in the surface unit cell, where f_j, $\mathbf{r}_j$, and u_j are the scattering factor, the position, and the isotropic vibrational amplitude (*7*), respectively, of surface atom j. The effect of anisotropic vibration is insignificant within measurement uncertainty and is therefore excluded in the calculations of the structure factor. The measured scattering intensity depends on the structure factor as well as beam intensity, sample-to-detector distance, and other factors (*8*).

Literature Cited

(1) Warren, B. E. *X-ray Diffraction*; Dover: New York, 1990.

(2) Robinson, I. K.; Tweet, D. J. Surface x-ray diffraction. *Rep. Prog. Phys.* **1992**, *55*, 599-651.

(3) Robinson, I. K. Crystal truncation rods and surface roughness. *Phys. Rev. B* **1986**, *33*, 3830-3836.

(4) Andrews, S. R.; Cowley, R. A. Scattering of x-rays from crystal-surfaces. *J. Phys. C. Solid State* **1985**, *18*, 6427-6439.

(5) Trainor, T. P.; Chaka, A. M.; Eng, P. J.; Newville, M.; Waychunas, G. A.; Catalano, J. G.; Brown, G. E. Structure and reactivity of the hydrated hematite (0001) surface. *Surf. Sci.* **2004**, *573*, 204-224.

(6) Trainor, T. P.; Eng, P. J.; Robinson, I. K. Calculation of crystal truncation rod structure factors for arbitrary rational surface terminations. *J. Appl. Crystallogr.* **2002**, *35*, 696-701.

(7) Effenberger, H.; Mereiter, K.; Zemann, J. Crystal-structure refinements of magnesite, calcite, rhodochrosite, siderite, smithonite, and dolomite, with discussion of some aspects of the stereochemistry of calcite type carbonates. *Z. Kristallogr.* **1981**, *156*, 233-243.

(8) Vlieg, E. ROD: A program for surface x-ray crystallography. *J. Appl. Crystallogr.* **2000**, *33*, 401-405.